The Rapid Imaging Planetary Spectrograph: Observations of Mercury's Sodium Exosphere in Twilight

Carl Schmidt, Jeffrey Baumgardner, Luke Moore, Thomas A. Bida, Ryan Swindle, Patrick Lierle

The Rapid Imaging Planetary Spectrograph: Observations of Mercury's Sodium Exosphere in Twilight

Carl A. Schmidt[1,2] , Jeffrey Baumgardner[1], Luke Moore[1], Thomas A. Bida[3], Ryan Swindle[4], and Patrick Lierle[1]
[1] Center for Space Physics, Boston University, 725 Commonwealth Ave., Boston MA 02215, USA; schmidtc@bu.edu
[2] LATMOS, Tour 45, Couloir 45-46, 4e étage (boîte 102), Université Pierre et Marie Curie, 4 place Jussieu, F-75252 Paris Cedex 05, France
[3] Lowell Observatory, 1400 W. Mars Hill Rd., Flagstaff, AZ 86001, USA
[4] Air Force Research Laboratory, 550 Lipoa Pkwy. # 100, Kihei, HI 96753, USA

Abstract

Ground-based observations of Mercury's exosphere are intrinsically difficult due to its proximity to the Sun and must be made in daylight or during brief windows at twilight. While the dimmer twilight background is far preferred, high airmass seeing and haze through Earth's atmosphere, windshake, and guiding all present formidable challenges toward spatially resolving the exosphere's structure. This study explores how such effects can be mitigated using results from a new instrument for high cadence spectroscopy, the Rapid Imaging Planetary Spectrograph. While high cadence observations do not significantly improve upon the resolution floor imposed by atmospheric seeing, the method does mitigate obstacles such as telescope tracking inaccuracy, windshake, and flux calibration. Whereas daytime observing has been the predominant methodology in past exosphere studies, the twilight observations performed here easily resolve distinct brightness enhancements near 50°–60° latitude, just equatorward of magnetic cusp regions. The exosphere in these locations is diagnostic of space weather effects such as charged particle precipitation. The structure in the sodium exosphere generally appears both more extended and brighter over the southern cusp, which has a broader open magnetic field line region. However, a northern enhancement during one observation confirms that the exosphere responds dynamically to environmental drivers, presumably changes in the solar wind dynamic pressure and/or interplanetary magnetic field.

1. Background

Mercury's exosphere offers insight into the composition of its topmost surface and the interaction of this surface with the local environment of interplanetary dust, neutral and charged particles, and intense sunlight. Sodium is thought to be both the dominant atom in Mercury's exosphere and the dominant planetary ion in its magnetosphere (Raines et al. 2015; Killen et al. 2019). Conveniently, Na is also the brightest spectroscopic emitter. While faint emissions of other species require off-disk observation, the several megaRayleigh Na D line emissions can be easily distinguished from the tens of MR/Å solar continuum that is scattered from the planet's dayside. Na emissions are therefore an important tool for understanding the interaction of Mercury's surface with its local environment.

Ground-based studies have largely reported that structure of the Na exosphere is episodic and enhanced at the poles (reviewed by Killen et al. 2007; McClintock et al. 2019). Early studies recognized polar enhancements as coupling between the exosphere and magnetosphere (Potter & Morgan 1990). It was later understood that such polar enhancements could also naturally track sources of locally enhanced Na abundance in surface mineralogy, since *the MErcury Surface, Space ENvironment, GEochemistry, and Ranging* (*MESSENGER*)

orbiter's Gamma Ray Spectrometer measurements have shown soil concentrations to increase at high latitudes, at least in the north (Peplowski et al. 2014). Still, the rapid morphology of polar exosphere spots on hourly or shorter timescales indicates that a magnetospheric driver such as ion sputtering is more likely responsible (e.g., Leblanc et al. 2009; Massetti et al. 2017; Orsini et al. 2018). Hemispheric traits in the Na^+ ion density suggest that the sunward, B_x, component of the interplanetary magnetic field regulates whether the polar Na exosphere is more enhanced in the north or the south (Jasinski et al. 2017). Such traits can be attributed to the neutral exosphere, since Na^+ originates solely as photoions and not directly from the surface via plasma sputtering (Raines et al. 2014).

The nature of polar enhancements in Mercury's exosphere remains unclear. On the one hand, multi-year surveys show no statistical evidence that sodium emissions are, on average, brighter in either hemisphere (Potter et al. 2006; Mangano et al. 2015). Yet, Na emissions over the southern magnetic cusp are frequently reported to be brighter than those in the north (Baumgardner et al. 2008; Leblanc et al. 2008; Mangano et al. 2013). This is perhaps a consequence of Mercury's offset magnetic dipole, which is predicted to channel four times more plasma precipitation to the southern surface than to the north (Anderson et al. 2011; Winslow et al. 2012). Also, the north–south asymmetry is typically inverted in the escaping neutral Na tail (Potter & Killen 2008), which is indicative of enhanced sources in the southern hemisphere (Schmidt 2013).

Ground-based evidence for dynamic magnetosphere–exosphere coupling seemingly contradicts the steady, seasonal repeatability of in situ Na data from *MESSENGER*'s Ultra Violet and Visible Spectrometer (UVVS). Cassidy et al. (2015, 2016) analyzed 10 Mercury years of equatorial limb scans of sodium with UVVS and found that the low-latitude exosphere exhibits a persistent seasonal variation markedly absent of sporadic changes. The Na column peaked at aphelion, surprisingly, where its solar-driven sources are weakest. Moreover, this enhancement evidently tracks the cold-pole longitudes: two geographic longitudes that alternately face the Sun at aphelion due to Mercury's 3:2 spin–orbit resonance. Two interpretations could plausibly explain such behavior. First, as a volatile, the sodium supply in the topmost soil could be sensitive to the maximum annual surface temperature. Na may have simply "baked-out" of the regolith grains, exhausting supplies in all but the coldest regions: high latitudes and cold-pole longitudes where surface temperatures peak ~130 K below their hot-pole counterparts. A second interpretation involves the bouncing and sticking of exospheric atoms over the surface. Cold-pole longitudes also locate at the terminators during perihelion. Solar-driven support of the exosphere peaks at perihelion and could send Na atoms bouncing across the ~700 K dayside until they stick to the first cold surface they encounter behind the terminator. Surrounding perihelion, Mercury revolves nearly as fast as it rotates, so the progression of local time nearly stands still and the solar sidereal motion even becomes slightly retrograde. The terminators remain at nearly fixed longitudes during 15% of Mercury's year surrounding perihelion, and so cold-trapping here could locally enhance the Na reservoir within the topmost regolith. Both scenarios could be causal to the cold-pole longitudinal enhancements that UVVS observed in the Na exosphere, and models have not yet determined which of these two influences dominates. It remains unknown if the Na soil concentration is enriched at cold-pole longitudes. Within the topmost few cm of soil, chemically analogous potassium is enhanced at the cold poles (Peplowski et al. 2012), but this trait could also be attributed to intrinsic composition since the K and non-volatile Mg/Si concentrations spatially anticorrelate (Weider et al. 2015).

Though the ground-based and *MESSENGER*-based results each paint significantly different portraits of the Na exosphere, both may be consistent knowing the limitations of each observer. Only UVVS equatorial limb scan observations have been analyzed so far. These view the exosphere facing northward from its orbital apoherm. This observing mode is ideal for exploring structure in local time, but these sight lines integrate though latitudinal structure and the bright planet itself obscures the polar exosphere. In turn, UVVS may have largely missed the brightest and most variable regions. The 1–2 hr duration of the UVVS limb scan observing sequence may have also exceeded timescales for variability, which could potentially be as short as ~10 minutes, the ballistic flight time characteristic of desorption. On the other hand, it is uncertain to what degree the variability and structure reported in multiple ground-based studies results from residual artifacts of seeing or the planet's disk within an intrinsically difficult observation. At least in low-latitude regions, the variability reported in multiple ground-based studies (Potter et al. 1999; Kameda et al. 2007; Mangano et al. 2015, etc.) is in disagreement with the seasonal UVVS results of Cassidy et al. (2015, 2016).

Twilight observations of Mercury are challenging due to fluctuations in seeing and atmospheric transmission on minute timescales as the sight line encounters haze layers near the horizon. Consequently, flux calibration cannot use standard stars, with the exception of wide-field coronagraphs that record field stars concurrently (e.g., Schmidt et al. 2010). Photometric models of Mercury itself must therefore be employed. Setting aside potential model inaccuracies (Domingue et al. 1997), such calibration must either integrate the entire disk emission or, in cases where only a portion of the disk is observed, have a metric for the instantaneous seeing, which subtends a sizable fraction of the planet's disk. Windshake can further exacerbate blurring on several second timescales. Slower pointing drift is often problematic as well. Pointing models can prove inaccurate at low altitudes because of telescope flexure, and closed-loop guiding may not be possible on such a bright, non-radially symmetric, extended target. Differential atmospheric refraction further complicates pointing, since the guider and spectrograph must operate at similar wavelengths to refract equally within arcsecond scale length tolerances. Guide cameras on most spectrographs operate independently of the spectral detector, introducing ambiguity when cross-referencing their exposures as a result of the aforementioned issues. Due to the challenges at twilight, solar telescopes have been a prominent tool in ground-based Mercury studies, despite the added background of the daytime sky spectrum.

To combat these challenges, the observational study herein explores a new technique for measuring the exosphere above Mercury's bright disk. Section 2 provides a description of the instrument. Observations made during three observing runs in 2018 are described in Section 3, and their analyses described in Section 4. Section 5 contains the primary observational results, and Sections 6 and 7 offer interpretations and conclusions, respectively.

2. RIPS Instrument Design

The Rapid Imaging Planetary Spectrograph (RIPS) was designed to produce a long-slit high-resolution spectrum and monochromatic image concurrently on the same detector, so that spectroscopy is paired with an unambiguous reference for pointing, blurring effects and relative flux. An Andor iXon 1024 × 1024 electron multiplying charge-coupled device (EMCCD) records both an image and a spectrum at fast frame rates up to 30 fps. Four motors within RIPS control echelle grating angle, slit width, and focus settings for both spectral and imaging channels. Typical Mercury observations would have the slit-aligned with the planet's spin axis. To set the position angle of the slit accordingly, the entire instrument can be rotated about its optical axis using an additional motor and gear train.

The optical path exiting the telescope first encounters an 18 Å FWHM pre-filter, which minimizes off-band light from entering the instrument and being scattered within. The telescope's first image lies at the spectrograph slit plane. After reflection from the slightly tilted slit jaws, the light passes through filters mounted in a 5 position filter wheel. One set of filters in this wheel is a 0.1 transmission neutral density filter sandwiched with a 4 Å equivalent width filter centered on Na D2. These two filters are necessary to keep the flux in the imaging channel close to the values seen in the spectral channel, as both images will be recorded simultaneously on the same CCD. This also insures that the image channel and the spectral channel are seeing Mercury at the same wavelength,

Table 1
Alkali Exosphere Observations with RIPS in 2018

UT Start (2018)	Airmass	N_{frames}	Exp (s)	Filter	Mode	Notes
03–15 1:47:06–1:54:08	3.90–4.30	17 × 100	0.05	Na	EMCCD	Evening 1.8 m
03–15 1:55:51–1:58:29	4.41–4.59	11 × 100	0.05	K	EMCCD	
06–21 5:33:03–5:39:10	5.52–6.28	2 × 500	0.5/1.0	Na	EMCCD	Evening 3.7 m
06–21 5:48:58–5:53:58	7.99–9.25	2	200	Na	Conventional	Anti-sunward
06–22 5:31:35–5:42:30	5.37–6.78	7	100	K	Conventional	
06–22 5:45:25–5:55:50	7.46–9.81	3	300	K	Conventional	Anti-sunward
06–23 5:33:30–5:40:24	4.90–5.58	5 × 100	1	K	EMCCD	Drift Scan
06–23 5:48:18–6:00:36	6.61–9.21	7 × 100	1	Na	EMCCD	Drift Scan
06–24 5:46:56–5:50:48	5.99–6.53	2	200	K	Conventional	
06–24 5:55:06–5:58:37	7.24–7.95	2	200	Na	Conventional	
06–24 6:03:48–6:07:16	9.25–10.37	2	200	K	Conventional	
06–26 5:54:11–5:57:50	6.24–6.79	3 × 100	1	K	EMCCD	
06–26 6:02:00–6:11:02	7.55–9.86	6 × 100	1	Na	EMCCD	
12–12 15:36:14–15:47:11	12.80–8.69	7 × 100	1	Na	EMCCD	Morning 3.7 m
12–12 15:51:11–16:25:29	7.75–4.00	5 × 100	5	K	EMCCD	
12–13 15:38:51–15:49:23	11.46–8.11	7 × 100	1	Na	EMCCD	
12–13 15:54:06–16:02:29	7.15–5.91	2 × 100	5	K	EMCCD	
12–13 16:12:07–16:20:45	4.91–4.28	5	100	K	Conventional	
12–13 16:22:49–16:29:59	4.15–3.76	3	200	K	Conventional	

eliminating any differential refraction concerns in their relative pointing.

Light passing through the slit aperture continues to a flat folding mirror, which directs the diverging beam into a collimating lens. Once dispersed by an echelle grating, the beam passes back through this collimating lens (now acting as an objective lens), and is directed to a field lens where the first image of the spectrum is formed. In this arrangement, the echelle grating is operating within only ~1°.5 of Littrow (where incidence and diffraction angles are identical). It yields a 24.6 mÅ pixel^{-1} dispersion at sodium wavelengths corresponding to 1.25 km s^{-1} pixel^{-1}. Rather than cross-dispersion, a given echelle order is isolated using a ~35 Å sorting filter mounted in a second 5 position filter wheel. Spectral resolving powers of up to $R = 97,000$, a 2.45 pixel FWHM, are achieved with the narrowest ~20 μm slit width. Although the pre-filter is, in principle, redundant with the Na filters in both instrument channels, internal reflections permit ample stray light to warrant its implementation despite the anti-reflection coated optics.

3. Observations

Three observational campaigns were completed during 2018 solar elongations: one at the 1.8 m Perkins telescope (Anderson Mesa, Arizona) and two at the 3.7 m Advanced Electro Optical System (AEOS) telescope (Haleakalā, Hawaii). Table 1 lists the data acquired. On each date, the observing sequence split the available time in order to target both sodium and potassium emissions. RIPS' CCD detector can operate in conventional or electron-multiplying modes and only sodium EMCCD mode observations are presented here. During the first light observations in Arizona, the telescope pointing was offset only once, as Earth's atmosphere, windshake, and pointing drifts otherwise provided the 4″ of motion needed for the slit to fully sample the planetary disk. AEOS, on the other hand, locked onto a fixed image of the disk using adaptive optics, requiring the slit aperture to be manually scanned across the planet's disk. To achieve this, RIPS was pivoted on a stage,
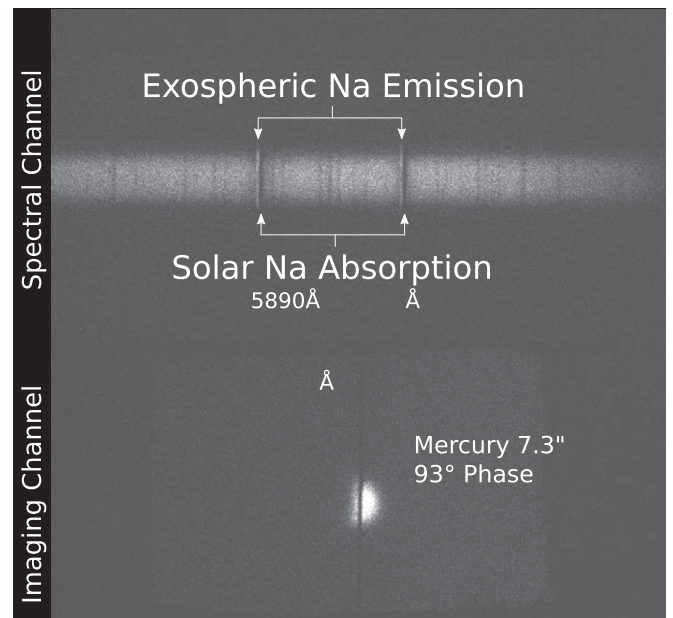
Figure 1. Example of a raw 0.05 s frame from first light at the Perkins 1.8 m telescope. One thousand seven hundred such frames were taken over 7 minutes, sufficient to characterize the exosphere during the brief observing window at twilight. During this time, the slit sampled most of the disk due to wandering of the planet's image. The online version of this figure offers an animation of matching frame rate, where frames are binned 2 × 2 to conserve file size. The real time duration of the video is 85 s.

(An animation of this figure is available.)

except on June 23 when we employed drift scans without tracking or adaptive optics.

An example RIPS frame appears in Figure 1. Its spectral range spans only 25 Å. With 12% magnification, the spectral channel is a highly dispersed mirror image of the light that passed through the slit aperture in the imaging channel. The imaging channel's plate scale amply samples the point-spread function at 0″.106 pixel^{-1} at Perkins and 0″.045 pixel^{-1} at AEOS. Mercury's exospheric emission can be seen to be

blueshifted from the solar absorption owing to its heliocentric velocity.

## 4. Photometric Modeling and Analysis

A photometric model of Mercury's surface reflectance is central to the RIPS data analysis. The formulation of Hapke (2012, their Equation (12.55)) is applied using parameters that Domingue et al. (2016) fit to the *MESSENGER* Mercury Dual Imaging System (MDIS) data set. Basic Hapke parameters are interpolated from MDIS' filter wavelengths to 5893 Å. Reflectivity is calculated for the instantaneous observing geometry, using the instrumental plate scale and Mercury's angular size to determine the bidirectional reflectance at each pixel. The product of this reflectance and the solar spectral irradiance, given Mercury's instantaneous heliocentric range and velocity, then determine the disk's theoretical brightness at a given pixel and wavelength. For convenience, this photometric model is rotated into plane-of-sky coordinates (celestial north as vertical, west as horizontal).

Standard bias and flat corrections are made to both RIPS channels. Files are normalized for exposure time and the imaging and spectral channels are each written to data cubes for independent processing. First, the imaging channel is transposed and rotationally aligned into plane-of-sky coordinates. The sole observation from the Perkins telescope was taken with two different slit position angles. As an az-alt telescope, AEOS delivers an image that rotates during the course of the observations. After bilinear interpolation across the slit, rotation angle is determined by cross-correlating the imaging channel with the photometric model blurred by an initial seeing estimate. After rotational alignment, frames are then translationally co-aligned to the blurred photometric model. Since co-alignment about the Mercury–Sun axis depends on atmospheric seeing, this alignment routine also blurs the model with a range of seeing conditions using Gaussian convolution kernels. When the correlation matrix between the imaging channel and blurred photometric model is maximized, a downhill simplex algorithm (e.g., Nelder & Mead 1965) returns an estimate of the instantaneous effective seeing and the cardinal direction alignment for each frame.

Rotational and translational alignments determined from the imaging channel are applied to the one-dimensional spectral channel, thereby filling in a monochromatic image using the planet's motion relative to the slit aperture. A solar spectrum is matched in resolution and fit to the observed continuum at each spatial pixel. The residual is summed over linewidth to extract the sodium signal in each frame. This one-dimensional total of the exospheric counts must then be spread over the two-dimensional region subtended by the slit's width. This is done using weighting from a normal probability distribution, which well represents the line spread function since the slit is unresolved. Frames are combined as the weighted arithmetic mean of a stack of exposures

Effective seeing, that is, seeing convolved with instrumental point-spread function, is applied as a metric for acceptance/rejection of individual frames. Frames with effective seeing above a specified threshold in Figure 2 are zero-weighted. The concept here is that occasional frames could, for a fraction of a second, capture images through minimal atmospheric turbulence and begin to approach a diffraction-limited image quality (e.g., Fried 1978). Figure 2 compares effective seeing with and without adaptive optics. Histograms based on measured blurring in the imaging channel show, perhaps unsurprisingly,
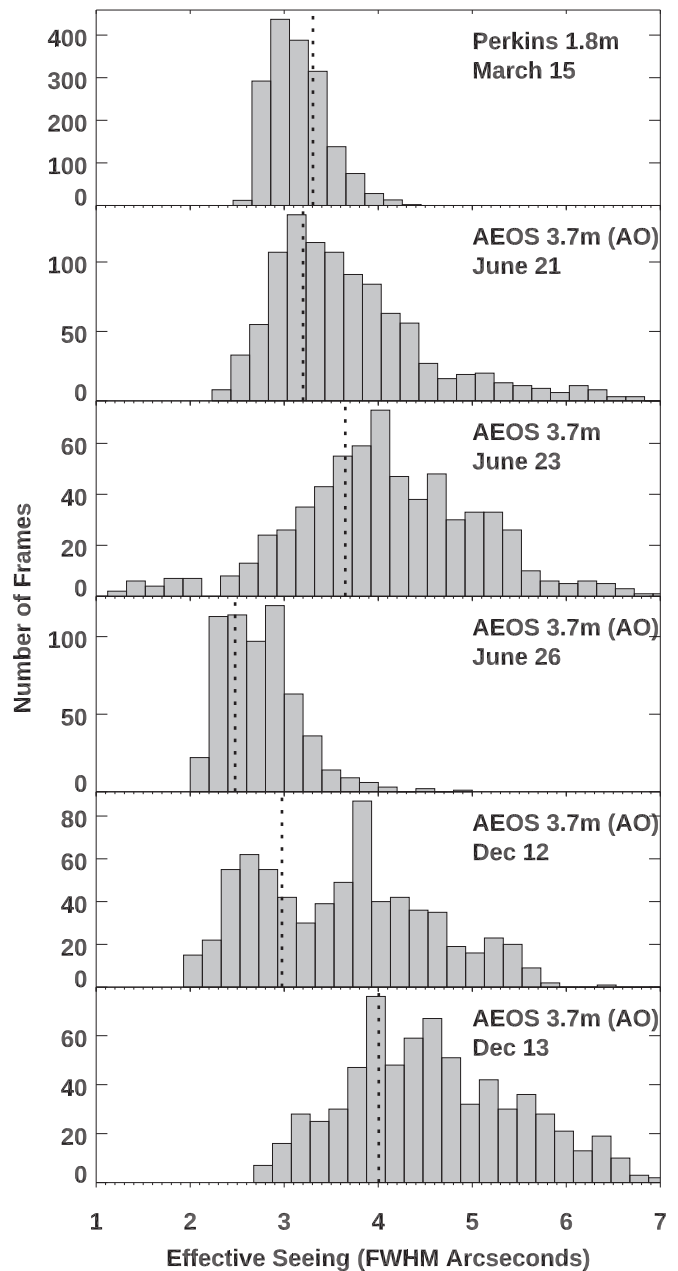

Figure 2. Histograms of empirical point-spread function widths for the RIPS imaging channel EMCCD measurements. Both conventional and adaptive optics configurations are shown. Vertical dotted lines represent the accept–reject thresholds used throughout this study. See Table 1 for airmass.

that turbulence levels during first light at the Perkins 1.8 m were largely homogeneous in the 3.9–4.3 airmass range. Subsequent nights at the AEOS 3.7 m demonstrate that it was also challenging for adaptive optics to correct wavefront distortions during those observing conditions. An often improved, but much a broader range of effective seeing values was measured with adaptive optics, largely due to conditions of atmospheric haze and the still higher airmass.

Flux calibration is performed by summing over a 1 Å region of continuum and processing it alongside the integrated brightness of the combined Na D_1 and D_2 exosphere lines. The sensitivity in Rayleighs/DN/s is taken to be the brightness of the photometric model divided by the recorded continuum.
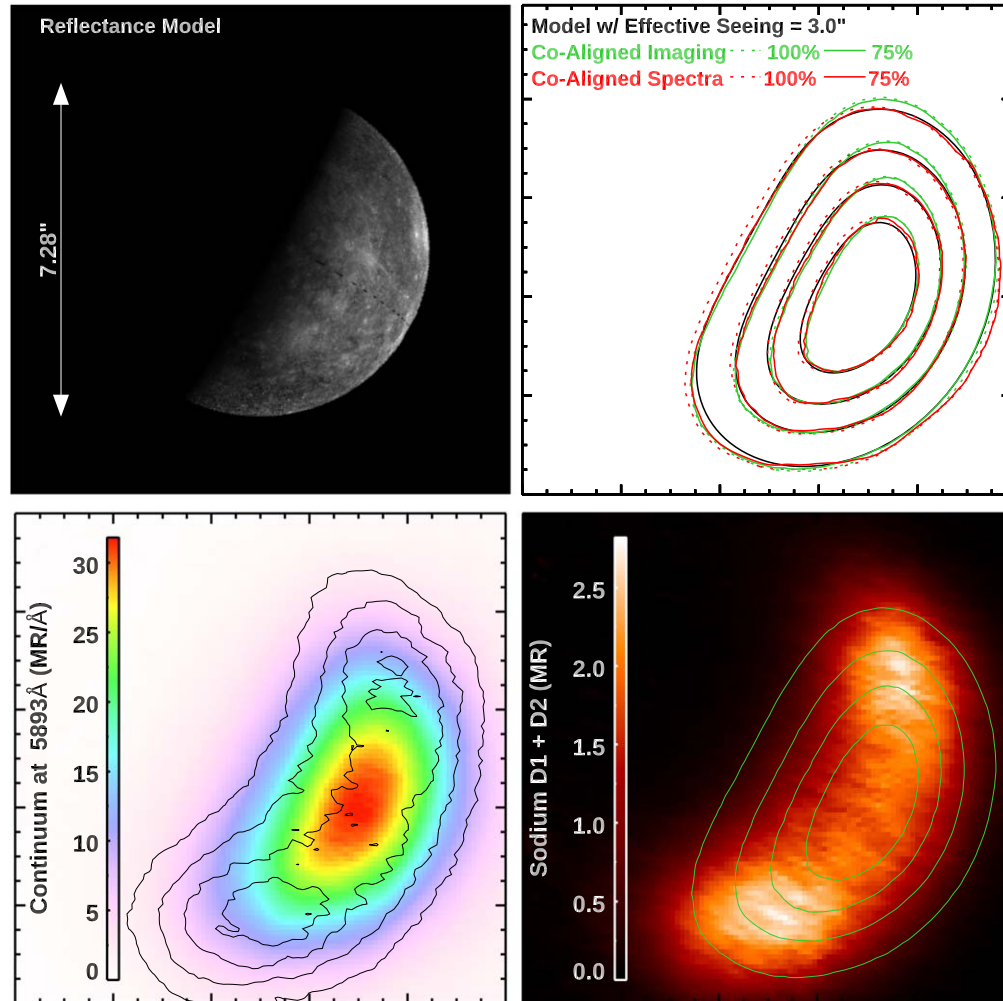
Figure 3. First light RIPS observations at the 1.8 m Perkins telescope in Arizona. Top left: a photometric model (Domingue et al. 2016), matched to the observing geometry with a global mosaic from *MESSENGER* MDIS overlaid. Top right: 20%, 40%, 60%, and 80% contours interval showing this photometric model convolved with a Gaussian kernel (black), the co-added and aligned imaging channel (green), and the image reconstructed by extracting, shifting, and averaging 1 Å of continuum in the spectral channel (red). As in Figure 2, downselecting a subset of frames below a threshold in effective seeing yields modest improvement, but >75% must be kept on this date in order to retain full spatial sampling across the planetary disk. Bottom left: a color image of this spectral reconstruction, with extracted sodium exosphere emission overlaid as contours. Bottom right: map of the exospheric Na radiance after a normalization for instrumental differences between the imaging and spectral channels. Contours of continuum scattered from the dayside surface are overlaid in green and have been processed in parallel to preserve relative spatial information.

Multiplying this sensitivity by the exosphere maps reconstructed from the spectral channel then flux-calibrates the data. Since both the continuum and photometric model are spatially integrated over the entire disk, this calibration is independent of the effective seeing, at least at the global level. Most importantly, the continuum images are an identically matched reference for the spatial reconstruction of the exosphere images, leaving no ambiguity about the quality of the spatial information obtained or processing artifacts from improper alignment. The absolute flux of the exosphere can finally be reduced to column density using standard calculations of the sodium excitation rate by solar photons (e.g., Killen et al. 2009).

5. Results

Figure 3 shows results from the instrument's first light observations. The photometric model with an overlaid *MESSENGER* MDIS low incidence angle mosaic is shown in the top left panel. The top right panel shows contours of this photometric model blurred by 3″, which is the mean effective seeing within the 75% sharpest images per Figure 2. Green and red contours for the imaging and spectral channels, respectively. Only marginal improvement from downselecting is seen. Dotted and solid contours nearly overlap, delineating the 75% best and "no rejection" cases. The image reconstructed from 1 Å of continuum in the spectral channel is shown at bottom left, with black Na emission contours overlaid. The bottom right panel shows this sodium emission, after a subtle correction that normalizes the spectral channel's reconstruction to match the imaging channel. 3 MR Na emission levels of the D line doublet are broadly consistent with prior disk-averaged data sets at this season (e.g., Leblanc & Johnson 2010). Enhancement over both poles is evident. The southern polar region is both brighter and more extended than the north. A relative deficiency of sodium at low latitudes is evident by
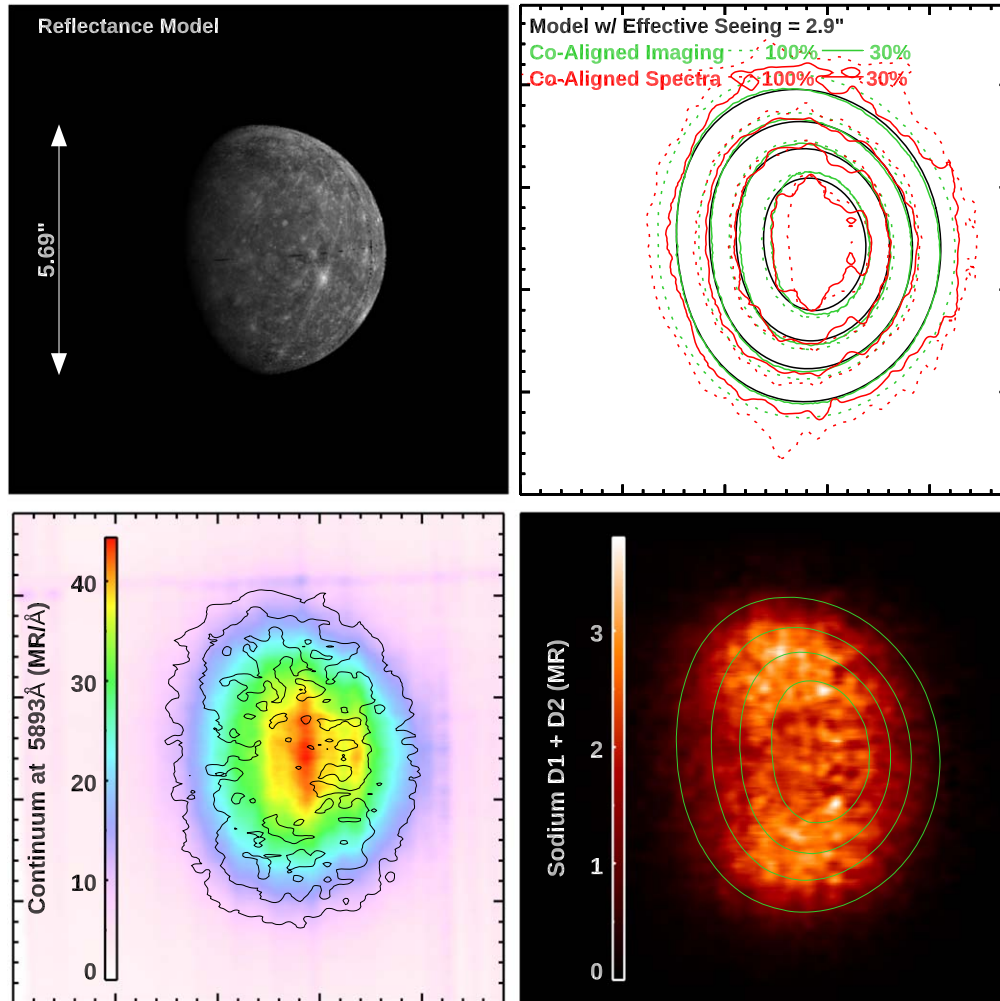
Figure 4. Observations from the AEOS telescope in Haleakalā, showing a brighter northern enhancement in the exosphere's emission.

comparing continuum the reflected by the planet's surface contours in green. Fainter Na near the panel's center at the dawn terminator results partly from a face-on viewing angle, as opposed to some higher slant column through the exosphere. Still, the exosphere's subsolar content is relatively weak, particularly considering Mercury is less than five days from its perihelion.

Lower image quality in Figure 4 is seen relative to Figure 3. Although a similar mean effective seeing is contained within a 30% threshold, fewer frames are accepted and the 22% smaller angle subtend by the disk is more susceptible to blurring. Additionally, the 2.35× magnified plate scale at AEOS requires more steps for the slit aperture to scan the disk. The more jagged red contours in spatial reconstructions derived from the spectral channel result from effective seeing variations as the slit is scanned and the fewer samplings per unit area of the disk. This is an instrumental effect, which is corrected by dividing the spectral image reconstruction by the imaging channel. Despite the poor image quality, polar enhancements are still recognizable. This June 21 measurement uniquely shows emissions that are brighter by a few percent in the northern hemisphere compared to the south when spatially integrated. Better image quality in Figure 5 shows the southern

enhancement was restored within a few days, at which time the 0.7 north/south ratio was the most significant asymmetry that RIPS recorded. Together, these observations suggest the polar exosphere is dynamic, at least on timescales of a few days. Polar enhancements also appeared when viewing the planet's evening hemisphere. Figure 6 shows dusk-side structure that is similar to the dawn-side in Figure 3. Observations on June 23 and December 13 also yielded similar structure to Figures 5 and 6, but with a lower spatial resolution.

6. Exosphere Structure and Column Density

All of the reconstructed exosphere maps show brightest emissions near the poles rather than low latitudes. This context is important for comparisons with UVVS orbital data, which made limb scans with minimum tangent altitudes almost exclusively within the 45°S to 35°N low-latitude range (see Cassidy et al. 2015, their Figure 3). Five of the six measurements that RIPS made in 2018 show a southern enhancement, as anticipated for sourcing driven by plasma precipitation. Yet, the north/south emission ratio is far less pronounced than ion sputtering would generally forecast. In peak emission as well as hemispheric averages, a factor of ∼1.4

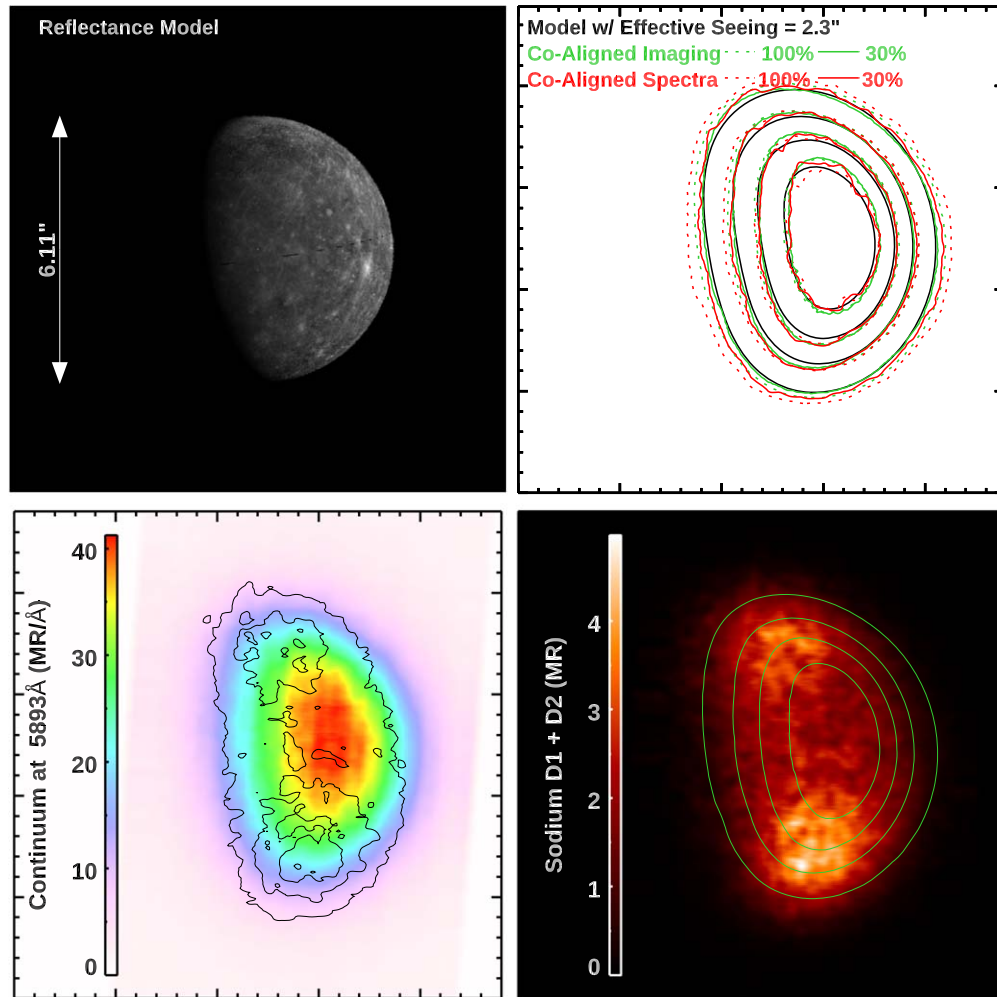# RIPS --- 2018-06-26 06:02 --- True Anomaly 104.7°

Figure 5. Same as Figure 4, exhibiting a brighter southern enhancement several days later.

southern enhancement over the north is the greatest that RIPS observed, while southern cusp precipitation is predicted to occur over a four times greater surface area (Winslow et al. 2012). The median enhancement RIPS measures is close to 1.2 south-to-north, which is consistent with past adaptive optics measurements by a fiber-fed instrument at AEOS (Baumgardner et al. 2008). Differing soil abundances at the cusp footprints could in principle account for this surprising near-symmetry in brightness. Na soil abundance is a steep function of latitude, with its polar abundance nearly twice that near the equator, at least in the northern hemisphere where measurements exist (Peplowski et al. 2014). Still, the 11° difference in cusp latitude cannot reproduce the 1.2 ratio in the exosphere if one assumes the southern soil abundance follows that which *MESSENGER* GRS has measured in the north.

In so far as these spatial resolutions can distinguish, polar enhancements in the exosphere do not exhibit the northward offset that is inherent to the magnetosphere. Rather, locations of the exosphere's polar enhancements are nearly symmetric in their latitude and both spots appear equatorward of the magnetic cusp. Winslow et al. (2012) determined a central latitude for the cusps of 75°N and 64°S. To more accurately estimate and compare the exosphere's latitude, we attempt

some degree of basic image deconvolution. Since it is established that blurring with a Gaussian convolution kernel can approximately forward-model an image of the dayside, basic deconvolution of this same kernel can in principle attain higher spatial resolution in the exosphere.

Figure 7 shows two examples of RIPS data after multiple iterations of a maximum likelihood deconvolution algorithm (Varosi & Landsman 1993). The grayscale continuum image is again processed identically alongside the exosphere as a reference. Contours represent Na column density in units of $10^{10}\,cm^{-2}$. Size scales of the exosphere's structure are still unresolved here, so peak column densities near $1.5 \times 10^{11}\,cm^{-2}$ represent a lower limit. UVVS showed the dayside column in the equatorial region reaches $3 \times 10^{11}\,cm^{-2}$ tangent to the surface (Cassidy et al. 2015). With an atmospheric scale height of 90 km, resolving this exospheric structure is challenging from the ground. Further deconvolution iterations cannot improve these results as this increasingly produces artifacts in the continuum. The remaining blur, which cannot be corrected, shifts the apparent spot locations inward toward the planet, while their true distribution almost certainly peaks tangent to the limb and not above the disk. The highest Na concentrations of the exosphere fall near 50°–60° latitudes, equatorward of the magnetic cusps and the northern
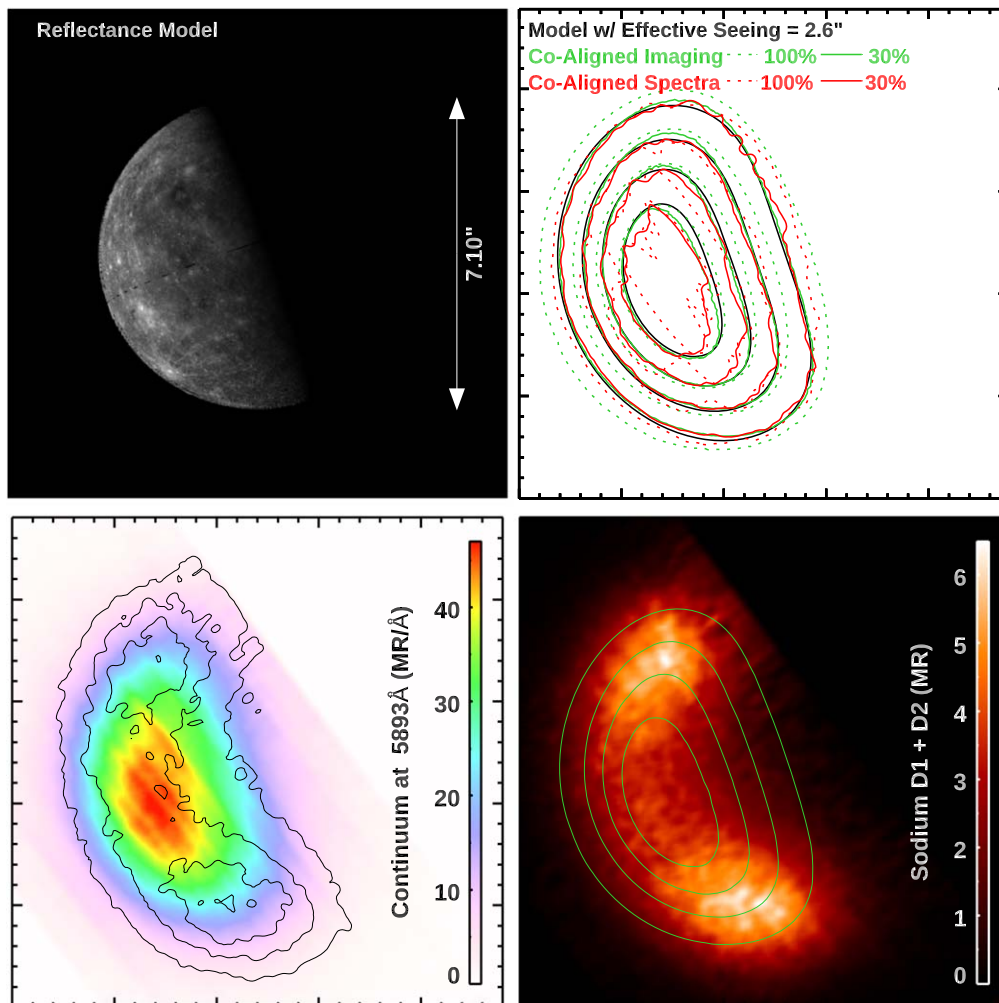
RIPS --- 2018-12-12 15:36 --- True Anomaly 76.5°

**Figure 6.** Same as Figures 4 and 5, but with viewing geometry facing the planet's evening hemisphere.

enhancement actually appears slightly equatorward of the south, counter to expectation (Anderson et al. 2011). The location of peak Na concentrations is broadly consistent with the mid-day local times expected for the magnetic cusp, but local time in this range cannot be determined precisely at phases near quadrature, a geometry inherent to twilight observations. Potter et al. (2006) proposed that limb brightening and radiation pressure alone could produce apparent enhancements at Mercury's poles. Densest regions in Figure 7 are well equatorward of the polar limb brightening they proposed, confirming that these features indeed illuminate the loci of sodium production from the surface.

Observations herein targeted solar elongations at seasons with high Na scattering rates, which peak at 64° true anomaly angle (Smyth & Marconi 1995). In this geometry, cold-pole longitudes at 90° and 270° appear near the terminator. Red traces in Figure 7 show cold-pole longitudes, coinciding within 5° of the dawn/dusk terminator. This region's illumination is edge on and its slant column density appears face-on. Still, the equatorial cold-pole longitude shows a paucity of emission considering the broad longitudinal width of this strong seasonal effect that UVVS observed. Cassidy et al. (2016) reported the enhancement was most evident between mid-morning and mid-afternoon local times, but that the dayside column was denser

than cold-pole longitudes at perihelion. At present the absence of any cold-pole emission near the terminators in RIPS observations can only confirm that the cold-pole enhancement is dormant near perihelion, and a broader coverage of observing geometries is needed to describe the effect further. A detailed description of the nature of cold-pole structures in the Na exosphere remains enigmatic, but has potential to reveal a systemic understanding of its sources and sinks.

7. Conclusions

High cadence techniques can overcome many of the difficulties associated with twilight observations of Mercury's exosphere at high airmass, and offer a viable alternative to daytime observations. The exosphere exhibits clear enhancements of comparable brightness at high latitudes near mid-day local times. These polar enhancements are variable on time-scales shorter than the seasonal changes that *MESSENGER* has characterized at lower latitudes. On average, the exosphere's southern hemisphere is indeed brighter than the north, though not nearly to the extent predicted by plasma precipitation through the planet's offset magnetosphere. Moreover, the exospheric enhancements at each pole appear equatorward of

Na Column x 10^{10} cm^{-2} 2018-03-15 01:47   Na Column x 10^{10} cm^{-2} 2018-12-12 15:36
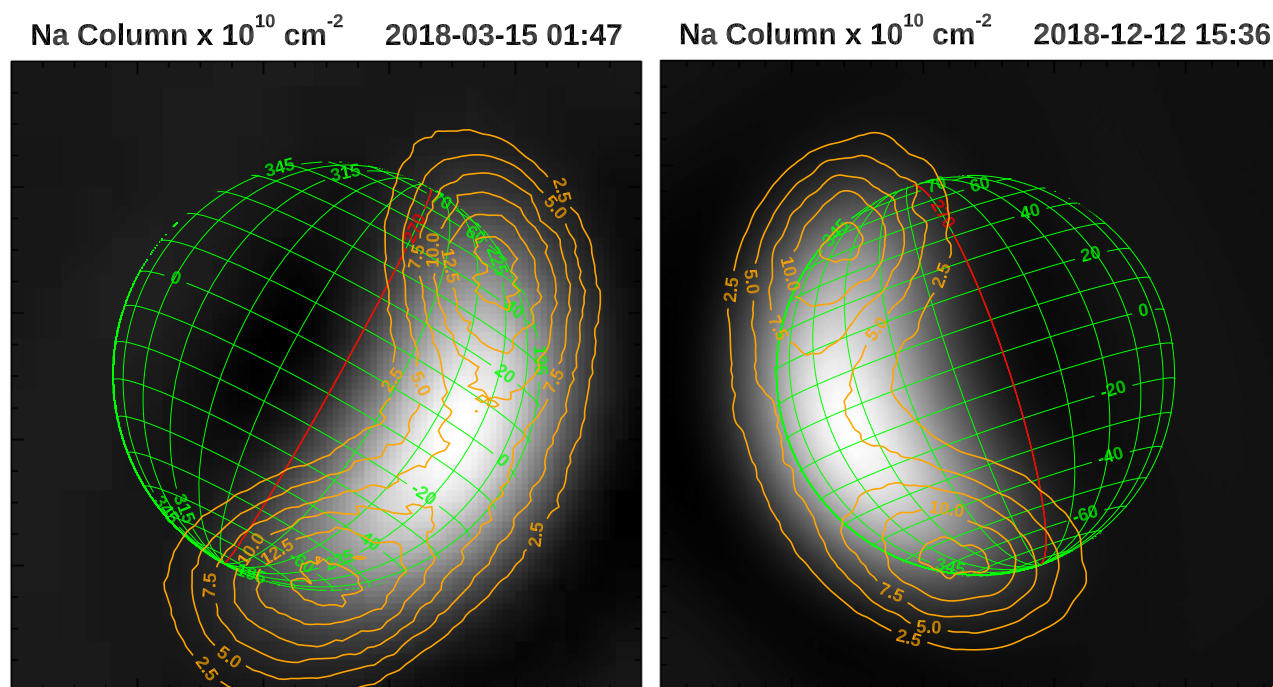
Figure 7. Maximum likelihood deconvolution of the continuum and Na exosphere maps in Figures 3 and 6. Iterations 17 and 9 iterations are applied, respectively. Gray shading represents continuum surface reflectance, processed in parallel. Contours give the Na column density in 10^{10} cm^{-2} units. The cold-pole longitudes, marked in red co-locate near the terminator.

the magnetic cusps and show latitudinal symmetry, with highest concentrations near 50°–60°.

8. Supplemental Materials

All data analyzed within this work is publicly archived at doi:10.5281/zenodo.3588493. IDL analysis software is publicly available at https://github.com/CarlSchmidt/RIPS-Pipeline.

ORCID iDs

Carl A. Schmidt https://orcid.org/0000-0002-6917-3458

References

Anderson, B. J., Johnson, C. L., Korth, H., et al. 2011, Sci, 333, 1859
Baumgardner, J., Wilson, J., & Mendillo, M. 2008, GeoRL, 35, L03201
Cassidy, T. A., McClintock, W. E., Killen, R. M., et al. 2016, GeoRL, 43, 121
Cassidy, T. A., Merkel, A. W., Burger, M. H., et al. 2015, Icar, 248, 547
Domingue, D. L., Denevi, B. W., Murchie, S. L., et al. 2016, Icar, 268, 172
Domingue, D. L., Sprague, A. L., & Hunten, D. M. 1997, Icar, 128, 75
Fried, D. L. 1978, JOSA, 68, 1651
Hapke, B. 2012, Theory of Reflectance and Emittance Spectroscopy (2nd ed.; Cambridge: Cambridge Univ. Press)

Jasinski, J. M., Slavin, J. A., Raines, J. M., et al. 2017, JGRA, 122, 12153
Kameda, S., Yoshikawa, I., Ono, J., et al. 2007, P&SS, 55, 1509
Killen, R., Cremonese, G., Lammer, H., et al. 2007, SSRV, 132, 433
Killen, R., Shemansky, D., & Mouawad, N. 2009, ApJS, 181, 351
Killen, R. M., Burger, B. H., Vervack, R. J., et al. 2019, in Mercury: The View after MESSENGER, ed. S. C. Solomon, L. R. Nittler, & B. J. Anderson (Cambridge: Cambridge Univ. Press), 407
Leblanc, F., Doressoundiram, A., Schneider, N., et al. 2008, GeoRL, 35, L18204
Leblanc, F., Doressoundiram, A., Schneider, N., et al. 2009, GeoRL, 36, L07201
Leblanc, F., & Johnson, R. E. 2010, Icar, 209, 280
Mangano, V., Massetti, S., Milillo, A., et al. 2013, P&SS, 82, 1
Mangano, V., Massetti, S., Milillo, A., et al. 2015, P&SS, 115, 102
Massetti, S., Mangano, V., Milillo, A., et al. 2017, GeoRL, 44, 2970
McClintock, W. E., Cassidy, T. A., Merkel, A. W., et al. 2019, in Mercury: The View after MESSENGER, ed. S. C. Solomon, L. R. Nittler, & B. J. Anderson (Cambridge: Cambridge Univ. Press), 371
Nelder, J. A., & Mead, R. 1965, CompJ, 7, 308
Orsini, S., Mangano, V., Milillo, A., et al. 2018, NatSR, 8, 928
Peplowski, P. N., Evans, L. G., Stockstill-Cahill, K. R., et al. 2014, Icar, 228, 86
Peplowski, P. N., Lawrence, D. J., Rhodes, E. A., et al. 2012, JGRE, 117, E00L10
Potter, A. E., & Killen, R. M. 2008, Icar, 194, 1
Potter, A. E., Killen, R. M., & Morgan, T. H. 1999, P&SS, 47, 1441
Potter, A. E., Killen, R. M., & Sarantos, M. 2006, Icar, 181, 1
Potter, A. E., & Morgan, T. H. 1990, Sci, 248, 835
Raines, J. M., DiBraccio, G. A., Cassidy, T. A., et al. 2015, SSRv, 192, 91
Raines, J. M., Gershman, D. J., Slavin, J. A., et al. 2014, JGRA, 119, 6587
Schmidt, C. A. 2013, JGRA, 118, 4564
Schmidt, C. A., Wilson, J. K., Baumgardner, J., et al. 2010, Icar, 207, 9
Smyth, W. H., & Marconi, M. L. 1995, ApJ, 441, 839
Varosi, F., & Landsman, W. B. 1993, in ASP Conf Ser. 52, Astronomical Data Analysis Software and Systems II, ed. R. J. Hanisch, R. J. V. Brissenden, & J. Barnes (San Francisco, CA: ASP), 33
Weider, S. Z., Nittler, L. R., Starr, R. D., et al. 2015, E&PSL, 416, 109
Winslow, R. M., Johnson, C. L., Anderson, B. J., et al. 2012, GeoRL, 39, L08112